Toxicology Letters 373 (2023) 160–171

Contents lists available at ScienceDirect

Toxicology Letters

journal homepage: www.journals.elsevier.com/toxicology-letters

# A novel binding site in the nicotinic acetylcholine receptor for MB327 can explain its allosteric modulation relevant for organophosphorus-poisoning treatment

Jesko Kaiser [a,1], Christoph G.W. Gertzen [a,2], Tamara Bernauer [b,3], Georg Höfner [b], Karin V. Niessen [c], Thomas Seeger [c], Franz F. Paintner [b,4], Klaus T. Wanner [b,5], Franz Worek [c], Horst Thiermann [c], Holger Gohlke [a,d,*,6]

[a] Institute for Pharmaceutical and Medicinal Chemistry, Heinrich Heine University Düsseldorf, Düsseldorf, Germany
[b] Department of Pharmacy – Center for Drug Research, Ludwig-Maximilians-Universität München, München, Germany
[c] Bundeswehr Institute of Pharmacology and Toxicology, München, Germany
[d] John von Neumann Institute for Computing (NIC), Jülich Supercomputing Centre (JSC), Institute of Biological Information Processing (IBI-7: Structural Biochemistry) & Institute of Bio, and Geosciences (IBG-4: Bioinformatics), Forschungszentrum Jülich, Jülich, Germany

ARTICLE INFO

Editor: Dr. Angela Mally

*Keywords:*
nAChR
Cooperativity
Bispyridinium compounds
Blind docking
Molecular dynamics simulations
Rigidity analysis

ABSTRACT

Organophosphorus compounds (OPCs) are highly toxic compounds that can block acetylcholine esterase (AChE) and thereby indirectly lead to an overstimulation of muscarinic and nicotinic acetylcholine receptors (nAChRs). The current treatment with atropine and AChE reactivators (oximes) is insufficient to prevent toxic effects, such as respiratory paralysis, after poisonings with various OPCs. Thus, alternative treatment options are required to increase treatment efficacy. Novel therapeutics, such as the bispyridinium non-oxime MB327, have been found to reestablish neuromuscular transmission by interacting directly with nAChR, probably via allosteric mechanisms. To rationally design new, more potent drugs addressing nAChR, knowledge of the binding mode of MB327 is fundamental. However, the binding pocket of MB327 has remained elusive. Here, we identify a new potential allosteric binding pocket (MB327-PAM-1) of MB327 located at the transition of the extracellular to the transmembrane region using blind docking experiments and molecular dynamics simulations. MB327 forms striking interactions with the receptor at this site. The interacting amino acids are highly conserved among different subunits and different species. Correspondingly, MB327 can interact with several nAChR subtypes from different species. We predict by rigidity analysis that MB327 exerts an allosteric effect on the orthosteric binding pocket and the transmembrane domain after binding to MB327-PAM-1. Furthermore, free ligand diffusion MD simulations reveal that MB327 also has an affinity to the orthosteric binding pocket, which agrees with recently published results that related bispyridinium compounds show inhibitory effects via the orthosteric binding site. The newly identified binding site allowed us to predict structural modifications of MB327, resulting in the more potent resensitizers PTM0062 and PTM0063.

## 1. Introduction

Despite the aim to ban chemical warfare agents, they remain a serious threat to the military and civilian population (Wiener and Hoffman, 2004). The highly toxic organophosphorus (OPCs) nerve agents block acetylcholinesterase (AChE) and lead to an increase of

* Correspondence to: Universitätsstr. 1, 40225 Düsseldorf, Germany.
*E-mail address:* gohlke@uni-duesseldorf.de (H. Gohlke).
[1] ORCID: 0000-0002-6429-0911
[2] ORCID: 0000-0002-9562-7708
[3] ORCID: 0000-0001-9570-1253
[4] ORCID: 0000-0002-6795-586X
[5] ORCID: 0000-0003-4399-1425
[6] ORCID: 0000-0001-8613-1447

https://doi.org/10.1016/j.toxlet.2022.11.018
Received 7 October 2022; Accepted 25 November 2022
Available online 26 November 2022

acetylcholine at cholinergic synapses, followed by overstimulation of muscarinic (mAChR) and nicotinic (nAChR) acetylcholine receptors. This is associated with several serious toxic effects, such as respiratory paralysis, which can lead to death (Wiener and Hoffman, 2004; Holmstedt, 1959).

So far, the treatment of OPC-poisonings mainly focuses on reestablishing the function of AChE with oximes and competitive antagonism at mAChR (Thiermann et al., 2013). Although oximes can have a remarkable positive indirect effect on nAChR function by restoring AChE functionality in poisonings with several OPCs, they lack efficacy with others, e.g., tabun- and soman-inhibited AChE, which results in a substantial therapeutic gap (Worek et al., 2004). Novel therapeutic approaches focus on ligands that interact directly with nAChR (Sheridan et al., 2005; Turner et al., 2011). As such, the bispyridinium compound MB327, which modulates several nAChR subtypes from different species, has been reported to reestablish neuromuscular transmission in vitro (Seeger et al., 2012; Niessen et al., 2016; Scheffel et al., 2018; Sichler et al., 2018). Furthermore, it leads to increased protection against soman-poisoning in guinea pigs in combination with hyoscine and physostigmine (Turner et al., 2011). However, to improve the efficacy of such compounds in a knowledge-driven molecular design workflow, detailed information of the binding mode is of utmost importance.

So far, three potential binding sites for bispyridinium compounds have been reported in nAChR. Based on blind docking experiments, Wein et al. suggested two potential binding sites of MB327, one in the extracellular domain and one in the upper part of the transmembrane domain (Wein et al., 2018). Recently, Epstein et al. proposed that bispyridinium compounds can bind in the orthosteric binding pocket and its neighboring region between the α- and ε-subunits, exerting an inhibitory effect, and confirmed their *in silico* findings using mutational studies (Epstein et al., 2021). Although this data explains the inhibitory effect of bispyridinium compounds, our previous studies indicated that MB327 probably acts as an allosteric modulator to reestablish muscular function (Niessen et al., 2018). Furthermore, the affinities of analogs of the bispyridinium compound SAD-128 to the orthosteric binding pocket do not correlate with the improvement of neuromuscular transmission, suggesting that this effect is not mediated via binding to the orthosteric binding site (Niessen et al., 2011). Additionally, the displacement of the orthosteric ligand [$^3$H]epibatidine by MB327 results in an $IC_{50} > 100$ μM, although the affinity of [$^3$H]epibatidine to nAChR was already increased at lower concentrations of MB327 (Niessen et al., 2013). Finally, pharmacological effects have been recorded at low μM concentrations of MB327 in the presence of carbamoylcholine. In the absence of carbamoylcholine, no effect has been detected. The latter findings further indicate an allosteric effect (Niessen et al., 2016).

In this study, we describe a novel potential binding site for M327 in nAChR, termed MB327-PAM-1, which was identified by a combination of molecular docking experiments, molecular simulations, and rigidity analyses. To explore the ligand-receptor dynamics, we performed molecular dynamics (MD) simulations and identified important interactions of MB327 with the receptor. The interacting amino acids are highly conserved among different subunits and different species, which can explain the promiscuity of MB327 towards several nAChR subtypes in different species. Furthermore, constraint network analysis (CNA) reveals that MB327 can allosterically impact both the orthosteric binding pocket and the transmembrane domain after binding to MB327-PAM-1. Free ligand diffusion MD simulations imply that MB327 is also affine to the orthosteric binding site, which might contribute to the inhibitory effect on nAChR at higher concentrations (Scheffel et al., 2018; Niessen et al., 2018). Finally, based on the newly identified binding mode of MB327, we predicted structural modifications of MB327, resulting in the more potent resensitizers PTM0062 and PTM0063.

## 2. Materials and methods

### 2.1. Homology modeling

The homology models of nAChR were created using MODELLER, version 9.19 (Webb and Sali, 2016). For modeling the desensitized state of nAChR, we only included receptor structures of nAChRs where the transmembrane domain is resolved and that are described to be in a desensitized state. All receptors that, to the best of our knowledge, were available in the PDB at the point of model generation were included. Receptors deposited by Unwin et al. (PDB-IDs 2BG9 (Unwin, 2005), 4AQ5, and 4AQ9 (Unwin and Fujiyoshi, 2012)) were not considered because later structures and experiments showed that, due to low resolution, the structures were wrongly fitted in the transmembrane domain (Mnatsakanyan and Jansen, 2013; Morales-Perez et al., 2016). Furthermore, to neglect a bias of similar protein backbone conformations from one publication, we only included one structure from each publication. However, because all of these receptors show a resolution above 3.5 Å and we expect MB327 to bind in the extracellular domain, we also included the crystal structure of the acetylcholine-binding protein in complex with the partial agonist 4-OH-DMXBA (PDB-ID: 2WN9 (Hibbs et al., 2009)). Concluding, for the human desensitized muscle-type nAChR, the PDB structures 6PV8 (Gharpure et al., 2019), 5KXI (Morales-Perez et al., 2016), 2WN9 (Hibbs et al., 2009), and 6CNK (Walsh et al., 2018) were used as templates.

For the human α7-nAChR, the PDB structures 6PV8 (Gharpure et al., 2019), 5KXI (Morales-Perez et al., 2016), 2WN9 (Hibbs et al., 2009), 6CNK (Walsh et al., 2018), and 6UR8 (Mukherjee et al., 2020) were used as templates. While not stated explicitly in that publication, the cryoEM structure of the α4β2 nAChR in complex with the partial agonist varenicline (PDB-ID: 6UR8 (Mukherjee et al., 2020)) shows a transmembrane domain typical for the desensitized state (SI Fig. 1). Thus, after analyzing the transmembrane pore of this receptor, we also included the receptor in the later created alpha7 nAChR models.

For the human inactive muscle-type nAChR, the PDB structure 6UWZ (Rahman et al., 2020) was used as a template. This was, to the best of our knowledge, the only PDB structure of the inactive nAChR available in the PDB at the time of model generation. To compare the binding site of PNU-120596 in the human muscle-type nAChR with α7-nAChR, the structure of the α7-nAChR in complex with PNU-120596 was used as a template (PDB-ID: 7EKT (Zhao et al., 2021)).

The alignments were created using BLAST (Altschul et al., 1990) and verified using PROMALS3D (Pei et al., 2008). Water molecules and crystallization artifacts were removed. Amino acids at the N- and C-termini and in the intracellular loop not resolved in the templates were not included in the models. 50 models were generated for the human muscle-type and α7-nAChR, respectively, and the final model was selected based on the DOPE potential (Shen and Sali, 2006), TopScore (Mulnaes and Gohlke, 2018), and visual inspection. The selected homology models were protonated using PROPKA (Olsson et al., 2011; Sondergaard et al., 2011) as implemented in Maestro (Schrödinger, 2020) at a pH of 7.4, and the termini were capped with NME and ACE using Maestro (Schrödinger, 2020).

### 2.2. Docking

For the docking, 3D structures of the ligands were generated using Maestro (Schrödinger, 2020). MB327 was placed in the middle of the extracellular part of the pore so that we could generate a docking box including the extracellular part of the receptor (SI Fig. S2). The ligands were subsequently docked into the receptor using AutoDock3 (Morris et al., 1998) in combination with DrugScore$^{2018}$ (Dittrich et al., 2019) as the scoring function. During the docking, default parameters were used, with the exception that the margin of the box was set to 35 Å and the grid spacing to 1 Å.

MB327, PTM0062, and PTM0063 were also docked into the newly

identified binding pocket using FRED (OpenEye Scientific Software, 2020) with default parameters. Therefore, conformers of MB327 were generated using OMEGA (OpenEye Scientific Software, 2020) with default parameters. The receptor was prepared using MakeReceptor (OpenEye Scientific Software, 2020) with the highest-ranked pose of MB327 after the initial docking for each pocket, and the ligands were subsequently docked into the receptor. To avoid a bias of the placement of MB327 based on the initial dockings, no constraints for protein-ligand interactions were selected, resulting in an independent placement of the ligands in the newly identified pocket. The best poses were selected based on their docking scores and visual inspection. For MD simulations, nicotine was docked to the orthosteric binding pocket using the same two-step procedure. For the simulations with MB327 bound to all five subunits, nicotine was added to nAChR by aligning the PDB structure of the α3β4-nAChR (PDB ID 6PV7 (Gharpure et al., 2019)) to the models and subsequently minimized in the orthosteric binding site using SZYBKI (OpenEye Scientific Software, 2020).

### 2.3. Molecular dynamics simulations

The structures were embedded in a membrane consisting of 1-palmitoyl-2-oleoyl-*sn*-glycero-3-phosphocholine (POPC) lipids and solvated in a rectangular box of OPC water (Izadi et al., 2014) using Packmol-Memgen (Schott-Verdugo and Gohlke, 2019), with the edge of the box at least 12 Å away from the solute atoms. For the MD simulations with MB327 bound to all five subunits, sodium was placed in the pore by aligning the sodium ion from the human α3β4-nAChR (PDB ID 6PV7 (Gharpure et al., 2019)). For the free ligand diffusion MD simulations, ten independent simulation systems were generated by placing MB327 at random positions within the rectangular box.

The AMBER package of molecular simulation software (Case et al., 2005) and the *ff19SB* force field (Tian et al., 2020) in combination with the Lipid17 force field (Gould et al., unpublished) was used to perform MD simulations. Ligand charges were calculated using Gaussian16 (Frisch et al. 2016). The "Particle Mesh Ewald" method was used to consider long-range interactions; for all bonds involving hydrogens, the SHAKE algorithm was applied (Darden et al., 1993; Ryckaert et al., 1977). During the thermalization period, the time step was set to 2 fs with a direct-space, nonbonded cutoff of 9 Å. During the production runs, hydrogen mass repartitioning was used, and the time step was set to 4 fs with a direct-space, nonbonded cutoff of 8 Å (Hopkins et al., 2015).

Initially, a combination of steepest descent and conjugate gradient minimization was performed; positional harmonic restraints were applied to protein and bound ligand atoms and gradually reduced from 5 (25 for the simulation with MB327 bound to all subunits) to 0 kcal $mol^{-1}$ $Å^{-2}$. Next, the system was heated to 100 K during 50 ps (5 ps for the simulations of the docked structure) of NVT-MD (constant number of particles, volume, and temperature). Subsequently, 50 ps (115 ps for the simulations of the docked structure) of NPT-MD (constant number of particles, pressure, and temperature) were conducted to heat the system to 300 K. During these steps, harmonic restraints with a force constant of 1 kcal $mol^{-1}$ $Å^{-2}$ (25 kcal $mol^{-1}$ $Å^{-2}$ for the simulations with MB327 bound to all subunits) were applied to receptor and ligand atoms. The harmonic restraints were then gradually reduced to 0 kcal $mol^{-1}$ $Å^{-2}$ during NPT-MD simulations.

Thereafter, the production runs of 900 ns length for the free ligand diffusion MD simulations (100 ns for the simulations of the docked structure) were performed. Subsequently, the distances of the ligand to the receptor were analyzed using the *nativecontacts mindist* function as implemented in CPPTRAJ (Roe and Cheatham, 2013). Representative binding poses were created by clustering the frames using the k-means clustering algorithm as implemented in CPPPTRAJ (Roe and Cheatham, 2013). The RMSD of the heavy atoms of the protein and the ligands have been used as a cluster criterion. The backbone RMSD and electron density values of the system during MD simulations were computed using CPPTRAJ (Roe and Cheatham, 2013). We computed the effective binding energy of MB327 in each binding pocket using the MM-GBSA method in combination with the OBC implicit water model, as implemented in AMBER (Case et al., 2005; Onufriev et al., 2004; Miller et al., 2012). We calculated the mean over all replicas *x* in which MB327 stays stable in MB327-PAM-1 and the standard error of the mean (SEM) using the following equation as done previously (Twizerimana et al., 2020):

$$SEM_{all} = \frac{1}{x}\sqrt{\sum_{i=1}^{x} SEM_i^{\,2}}$$

### 2.4. Constraint network analysis (CNA)

Frames were extracted from the MD simulations of nAChR with MB327 bound to all five subunits and nicotine bound to both orthosteric binding sites every 1 ns using CPPTRAJ (Roe and Cheatham, 2013). To investigate a potential functional coupling between the ligand binding sites as well as with the transmembrane domain, we performed perturbation runs as implemented in CNA (Pfleger et al., 2013a). The perturbation approach performs two runs of constraint dilution simulations of the protein in the presence and absence of the ligands and, thereby, calculates a per-residue decomposition $\Delta G_{i,CNA}$ that indicates the ligands' effect on the structural stability of residue *i*. We performed three calculations, one where only MB327 was extracted from the system (s1), one where only nicotine was extracted (s2), and one where both ligands where extracted (s1/s2) to investigate the respective impact of the ligands. To investigate the statistical independence of the frames, we computed the autocorrelation function (ACF($\tau$)) of the first replica for $\Delta G_{CNA,s1}$ (Case et al., 2005). As ACF($\tau = 0.5$ ns) $= 0.2 < 1/e$, the frames are statistically independent. To predict cooperative effects in the system, $\Delta G_{CNA,\{s1/s2,\ s1,\ s2\}}$ was computed as the sum over all $\Delta G_{i,CNA}$ for the respective state. Then, the cooperative free energy $\Delta\Delta G_{CNA,n}$ was computed according to Eq. 1 as done previously (Pfleger et al., 2021),

$$\Delta\Delta G_{CNA,n} = \Delta G_{CNA,s1/s2} - (\Delta G_{CNA,s1} + \Delta G_{CNA,s2}) \quad (1)$$

where positive values indicate a negative cooperativity while negative values indicate a positive cooperativity.

To analyze the impact of calcium on the system, we removed the ligands from nAChR and performed two CNA runs, one where we manually added additional restraints in the form of covalent bonds between the two glutamates involved in calcium binding in three subunits, and one without additional restraints. The former mimics the local rigidifying effect of a bound calcium ion. Then, we calculated the difference in $\Delta G_{i,CNA}$ between the CNA analyses for the systems with and without additional restraints for each residue *i* to compute the impact of calcium on the structural stability of nAChR.

### 2.5. Similarity analysis of the binding pocket

For the similarity analysis of the binding pocket, the PDB structure 1UW6 (Celie et al., 2004) of the acetylcholine binding protein of *Lymnaea stagnalis* was aligned to the human muscle-type nAChR model using UCSF Chimera (Pettersen et al., 2004), and amino acids within 5 Å of nicotine were compared to the respective region in the δ-β-subunit using BLAST (Altschul et al., 1990).

### 2.6. Electrostatic analysis

The electrostatics was analyzed by solving the linear *Poisson-Boltzman* equation as implemented in APBS (Jurrus et al., 2018) using the APBS Pymol Plugin in the presence of positively (charge +1, ion radius 1.8 Å) and negatively (charge −1, ion radius 2.0 Å) charged counter ions in a concentration of 0.15 M. The dielectric constant of the solvent and the protein were set to 78.0 and 2.0, respectively.

### 2.7. Image generation

Images of nAChR were generated using PyMol (Schrödinger, 2015), version 2.3.0.

### 2.8. Analysis of the transmembrane pore radius

The transmembrane pore radius of proteins was analyzed using the CAVER PyMol Plugin (Pavelka et al., 2016).

### 2.9. Synthesis of PTM0062 (3a) and PTM0063 (3b)

Microwave reactions were carried out on a Discover SP microwave system by CEM GmbH. All chemicals were used as purchased from commercial sources. Solvents used for purification were distilled before use. $^{1}H$ and $^{13}C$ NMR spectra were recorded on a Bruker BioSpin Avance III HD 400. MestReNova (Version 14.1.0) from Mestrelab Research S.L. 2019 was used for data processing, and for calibration, the solvent signal was used. The purity of the test compounds was > 99 %, determined by means of quantitative NMR using TraceCERT® ethyl 4-(dimethylamino) benzoate from Sigma Aldrich as an internal calibrant (Cushman et al., 2014; Pauli et al., 2014). High-resolution mass spectrometry was performed on a Finnigan LTQ FT (ESI). Melting points were determined with a Büchi 510 melting point instrument and are uncorrected. For IR spectroscopy, an FT-IR Spectrometer 1600 from PerkinElmer was used.

#### 2.9.1. 4-Amino-1-{3-[4-(tert-butyl)pyridin-1-ium-1-yl]propyl}pyridin-1-ium diiodide (3a)

A solution of 4-(*tert*-butyl)− 1-(3-iodopropyl)pyridin-1-ium iodide (**1**) (Rappenglück, 2018) (216 mg, 0.500 mmol, 1.0 eq.) and pyridin-4-amine (**2a**) (51.8 mg, 0.550 mmol, 1.1 eq.) in acetonitrile (1 mL) was stirred under microwave irradiation (150 W) for 1 h at 90 °C. The reaction mixture was concentrated in vacuo and the residue purified by recrystallization from EtOAc/EtOH (2:3) yielding **3a** (215 mg, 82 %) as yellow solid. mp.: 205 °C; IR (KBr): $\tilde{\nu}$ = 3184, 1652, 1194, 839 $cm^{-1}$; $^{1}H$ NMR (400 MHz, $CD_3OD$): δ = 1.45 (s, 9 H, $C(CH_3)_3$), 2.58–2.70 (m, 2 H, $NCH_2CH_2$), 4.38 (t, *J* = 7.7 Hz, 2 H, $CH_2NCHCHCNH_2$), 4.75 (t, *J* = 7.8 Hz, 2 H, $CH_2NCHCHCC(CH_3)_3$), 6.82–6.90 (m, 2 H, $CHCNH_2$), 8.12–8.20 (m, 2 H, $CHCC(CH_3)_3$), 8.18–8.26 (m, 2 H, $CHCHCNH_2$), 8.93–9.00 (m, 2 H, $CHCHCC(CH_3)_3$); $^{13}C$ NMR (101 MHz, $CD_3OD$): δ = 30.22 [$C(CH_3)_3$], 33.11 ($NCH_2CH_2$), 37.66 ($C(CH_3)_3$), 55.54 ($CH_2NCHCHCNH_2$), 58.55 [$CH_2NCHCHCC(CH_3)_3$], 111.04 ($CHCNH_2$), 126.87 [$CHCC(CH_3)_3$], 144.08 ($CHCHCNH_2$), 145.39 [$CHCHCC(CH_3)_3$], 160.91 ($CNH_2$), 173.18 [$CCC(CH_3)_3$]; HRMS-ESI *m/z* $[M\text{-}I\text{-}]^+$ calcd for $C_{17}H_{25}N_3I$: 398.1093, found: 398.1082.

#### 2.9.2. 4-(tert-Butyl)− 1-[3-(4-(methylamino)pyridin-1-ium-1-yl]propyl) pyridin-1-ium diiodide (3b)

Synthesis according to the procedure described above for the preparation of **3a** from 4-(*tert*-butyl)−1-(3-iodopropyl)pyridin-1-ium iodide (**1**) (Rappenglück, 2018) (216 mg, 0.500 mmol, 1.0 eq.) and *N*-methylpyridin-4-amine (**2b**) (56.8 mg, 0.525 mmol, 1.05 eq.). Recrystallization from EtOAc/EtOH (2:1). **3b** (210 mg, 78 %). Yellow solid. mp.: 180 °C; IR (KBr): $\tilde{\nu}$ = 3013, 1654, 1194, 843 $cm^{-1}$; $^{1}H$ NMR (400 MHz, $CD_3OD$): δ = 1.45 [s, 9 H, $C(CH_3)_3$], 2.60–2.72 (m, 2 H, $NCH_2CH_2$), 2.99 (s, 3 H, $NCH_3$), 4.41 (t, *J* = 7.7 Hz, 2 H, $CH_2NCHCHCNHCH_3$), 4.78 [t, *J* = 7.8 Hz, 2 H, $CH_2NCHCHCC(CH_3)_3$)], 6.84–6.94 (m, 2 H, $CHCNHCH_3$), 8.13–8.22 [m, 3 H, $CHCHCNHCH_3$, $CHCC(CH_3)_3$], 8.33–8.40 (m, 1 H, $CHCHCNHCH_3$), 8.96–9.03 [m, 2 H, $CHCHCC(CH_3)_3$]; $^{13}C$ NMR (101 MHz, $CD_3OD$): δ = 29.80 ($NCH_3$), 30.23 [$C(CH_3)_3$], 33.19 ($NCH_2CH_2$), 37.65 [$C(CH_3)_3$], 55.39 ($CH_2NCHCHCNHCH_3$), 58.50 [$CH_2NCHCHCC(CH_3)_3$], 106.66 ($CHCNHCH_3$), 112.03 ($CHCNHCH_3$), 126.87 [$CHCC(CH_3)_3$], 142.39 ($CHCHCNHCH_3$), 144.92 ($CHCHCNHCH_3$), 145.40 [$CHCHCC(CH_3)_3$], 159.57 ($CNHCH_3$), 173.09 [$CCC(CH_3)_3$]; HRMS-ESI *m/z* $[M\text{-}I\text{-}]^+$ calcd for $C_{18}H_{27}N_3I$: 412.1250, found: 412.1230.

### 2.10. Rat diaphragm myography

All procedures using animals followed animal care regulations and were approved by the responsible ethics committee. Preparation of rat diaphragm hemispheres and experimental protocol of myography was performed as described before with slight modifications (Seeger et al., 2012, 2007). In short, for all procedures (including wash-out steps, preparation of soman and bispyridinium compound solutions) aerated Tyrode solution (125 mM NaCl, 24 mM $NaHCO_3$, 5.4 mM KCl, 1 mM $MgCl_2$, 1.8 mM $CaCl_2$, 10 mM glucose, 95 % $O_2$, 5 % $CO_2$; pH 7.4; 25 ± 0.5 °C) was used. After the recording of control muscle force, the muscle preparations were incubated in the Tyrode solution, containing 3 μM soman. Following a 20 min wash-out period, the test compounds PTM0062 or PTM0063 were added in ascending concentrations (1 μM, 10 μM, 100 μM, 300 μM). The incubation time was 20 min for each concentration. The electric field stimulation was performed with 10 μs pulse width and 0.2 A amplitudes. The titanic trains of 20 Hz, 50 Hz, 100 Hz were applied for 1 s and in 10 min intervals. Muscle force was calculated as a time-force integral (area under the curve, AUC) and constrained to values obtained for maximal force generation (muscle force in the presence of Tyrode solution without any additives; 100 %).

## 3. Results

### 3.1. Identifying a new potential binding site via blind docking

To identify a possible binding site of MB327 without bias towards any previously known binding site, we have used blind docking experiments. Here, binding to the complete extracellular domain and half of the transmembrane domain of the human adult muscle-type and the α7-nAChR was allowed (SI Fig. S2), as the permanently charged MB327 likely does not cross the plasma membrane in a notable quantity and, thus, likely does not interact with the intracellular parts of the receptor. Using AutoDock (Morris et al., 1998) and DrugScore$^{2018}$ (Dittrich et al., 2019), we docked MB327 100 times to each subtype. This allows us to judge whether MB327 prefers the orthosteric binding site or alternative ones. The largest cluster, which was also the cluster with the best-ranked docking pose, placed MB327 in both receptors in a newly identified binding pocket, MB327-PAM-1, which is located in between two adjacent subunits at the transition from the extracellular to the transmembrane domain (Fig. 1, Fig. 2A, SI Table S1, SI Table S2). Since the α7-nAChR is a homopentamer, there are five potential, identical binding sites for MB327. The human muscle type nAChR is a heteropentamer containing 2 $\alpha_1$, 1 $\beta_1$, 1 δ and 1 ε subunit. In 8 out of the 10 highest ranked clusters, MB327 binds to MB327-PAM-1 but in different subunits (SI Table S1) suggesting that MB327 can bind in the newly identified binding pocket between different subunits. By contrast, MB327 binds to the orthosteric binding site in the 28th and 34th highest ranked cluster only (SI Table S1). In comparison, in 58 out of 100 docking runs, including 30 poses in the highest ranked cluster, the orthosteric agonist acetylcholine was placed in the orthosteric binding pocket, confirming the quality of our predictions (SI Table S3).

### 3.2. MD simulations strengthen the suggestion of the new binding site

To consider receptor plasticity and assess the stability of the binding pose in the receptor, we performed 32 times 100 ns long MD simulations starting from the docked structure of MB327 in all five subunits of the human muscle-type nAChR embedded in an explicit bilayer membrane (SI Fig. S3). The initial blind docking procedure failed to place MB327 between the β- and α-subunit in the best 100 docked poses, however. Still, we expect that MB327 can bind in between all five subunits of the receptor because of the high sequence similarity of amino acids available for electrostatic interactions (Table 1). Hence, to enable simulations

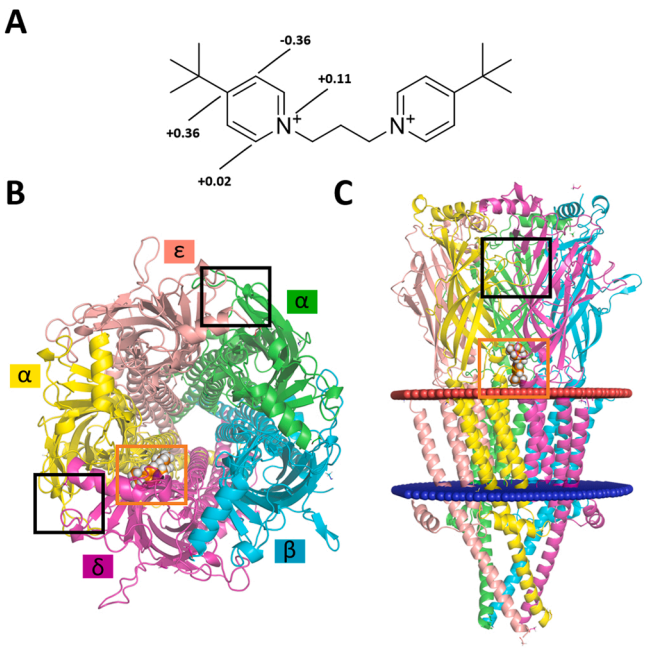


**Fig. 1.** Location of MB327-PAM-1 in the human adult muscle-type nAChR. (A) MB327 with restrained electrostatic potential (RESP) partial charges (Frisch et al., 2016; Bayly et al., 1993) of the nitrogen and carbons in the aromatic ring. nAChR is viewed from (B) the extracellular space and (C) the side. MB327 is displayed in orange spheres The orange box indicates the location of the newly identified allosteric binding site MB327-PAM-1. The orthosteric binding pocket is marked with a black box. The membrane is indicated with red (extracellular border) and blue (intracellular border) spheres. The membrane position was extracted from the α7-nAChR in a desensitized state (PDB ID 7KOQ (Noviello et al., 2021)) from the Orientations of Proteins in Membranes (OPM) database (Lomize et al., 2012).

with MB327 bound to all five subunits, we docked MB327 into MB327-PAM-1 between each subunit using FRED (OpenEye Scientific Software, 2020) (SI Fig. S4). Throughout the MD simulations, the receptor and the membrane remained structurally virtually invariant (SI Figs. S5, S6). To evaluate whether MB327 stays bound during the 100 ns long MD simulations, we evaluated the minimal distance of MB327 to the highly conserved isoleucine of β1 ($I61_{\alpha}$), located centrally in each respective subunit (Fig. 2A, SI Fig. S7). Since the largest distance among the docked structures in all five subunits of this isoleucine to MB327 is 4.2 Å (SI Table S4), we considered an unbinding of MB327 at distances above 5 Å. In 122 of 160 cases (32 replicas * 5 possible binding sites), MB327 stays bound in MB327-PAM-1. The unbinding events were mainly observed in between the β- and α-subunit (in 19/32 replicas) and in between the α- and ε-subunit (in 16/32 replicas), while we observed a rare unbinding in between the δ- and β-subunit (in 3/32 replicas) and no unbinding in between the α- and δ- as well as the ε- and α-subunit. This is in line with effective binding energy computations of MB327 in each subunit, revealing that MB327 binds most stably in between the α- and δ- ($-23.01 \pm 0.04$ kcal mol$^{-1}$) and ε- and α-subunit ($-24.43 \pm 0.05$ kcal mol$^{-1}$) and shows decreased free binding energies in between the δ- and β-subunit ($-19.2 \pm 0.05$ kcal mol$^{-1}$), the α- and ε-subunit ($-18.99 \pm 0.07$), and the β- and α-subunit ($-14.30 \pm 0.08$ kcal mol$^{-1}$).

We next analyzed striking interactions with the receptor in the three binding pockets where MB327 remained predominantly bound. To do so, we computed the minimal distance of acidic side chains of the receptor to the partially positively charged atoms in MB327 when MB327 was bound. Because the nitrogen is part of an aromatic ring, its positive charge can be delocalized among the ring members. In fact, restrained electrostatic potential (RESP) partial charges (Frisch et al., 2016; Bayly et al., 1993) revealed that the positive charge is mainly located on the nitrogen and the carbon atom in *para* position (Fig. 1 A). Thus, we analyzed the minimal distance of these two atoms in each ring to the oxygen atoms of acidic side chains located in the binding pocket in each subunit where MB327 stays stable during the simulations (Fig. 2B, C, D). In between the α- and δ-subunit, MB327 mainly shows interactions with $E210_{\delta}$ located in loop F (Fig. 2B). This amino acid is highly conserved among different subunits of the heteropentamer. However, in between the δ- and β-subunit, this residue is mutated to glutamine (Table 1). There, MB327 shows almost no interactions with the side chain oxygen of this residue (SI Fig. S8C). However, in this subunit, MB327 forms good interactions with $E71_{\delta}$ located in the β1-β2-loop (Fig. 2C). In between the ε- and α-subunit, glutamates are present at both positions ($E220_{\alpha}$ and $E68_{\varepsilon}$, Fig. 2A). However, MB327 shows preferred interactions with $E68_{\varepsilon}$ located in the β1-β2-loop (Fig. 2D, SI Fig. S8D).

These results suggest the two acidic glutamates as major interaction partners for MB327. Both acidic amino acids are highly conserved among similar binding pockets in different subunits and different species (Table 1). In each subunit, at least one of the two acidic amino acids is present to stabilize MB327 in the binding pocket, strengthening the assumption that MB327 can bind in all subunits. This is in line with reports that MB327 can bind to nAChR of different species, e.g., *T. californica*, and to nAChRs containing different subunits, e.g., human α7-nAChR (Turner et al., 2011; Seeger et al., 2012; Niessen et al., 2016; Scheffel et al., 2018; Sichler et al., 2018). However, in our MD simulations, MB327 did not stay stable in the proposed binding pocket in two out of five subunits. There, MB327 might not have been placed correctly during the initial docking. In fact, in the two binding sites where MB327 unbound faster, the partially positively charged atoms of MB327 were more than 5 Å away from the carboxyl oxygens of the described amino acids, whereas in the other subunits, the distance to at least one oxygen is 4.5 Å or less (SI Table S4). Unsurprisingly, the effective binding energy is worst in between the β- and α-subunit where the ligand was placed farthest from the two glutamates in the binding site (SI Table S4). This further stresses the importance of these two amino acids. Thus, mutating one of these amino acids should lead to a significant decrease in binding affinity.

### 3.3. *Allosteric impacts originating from the newly proposed binding pocket*

To probe if the newly identified binding pocket MB327-PAM-1 couples functionally with other parts of nAChR, we applied a model of dynamic allostery introduced by us (Pfleger et al., 2013a, 2021) that describes allosteric effects due to ligand binding in terms of a free energy measure $\Delta G_{i,\mathrm{CNA}}$ computed from changes in biomolecular statics via CNA. To generate conformational ensembles for the analyses, we used the 32 times 100 ns long MD simulations with MB327 bound to all five subunits and nicotine bound to both orthosteric binding sites of the human muscle-type nAChR. However, due to the instability of MB327 in two subunits, we only considered the three subunits where MB327 remained stable in MB327-PAM-1. In 29 simulations, all three MB327 molecules were still bound after 100 ns; these replica were used to analyze the allosteric effect of MB327 binding on nAChR. For the perturbation run in CNA, all three MB327 molecules were removed to investigate the allosteric impact due to the ligand. Furthermore, to study the cooperative behavior of both ligands, two additional perturbation runs were performed: first, both nicotine molecules were removed; second, all stably bound ligands (three MB327 ligands and two nicotine molecules) were removed (SI Fig. S9).

CNA reveals that MB327 binding structurally stabilizes the extracellular domain, including amino acids in the orthosteric binding pocket (Fig. 3A, SI Fig. S10.). Interestingly, MB327 shows the largest impact in the orthosteric binding site on $W169_{\alpha}$, the only residue forming a hydrogen bond to the orthosteric ligand nicotine in the PDB structure of the human α3β4-nAChR (PDB-ID 6PV7) (Gharpure et al., 2019). MB327 transmits its allosteric information to the extracellular domain via both

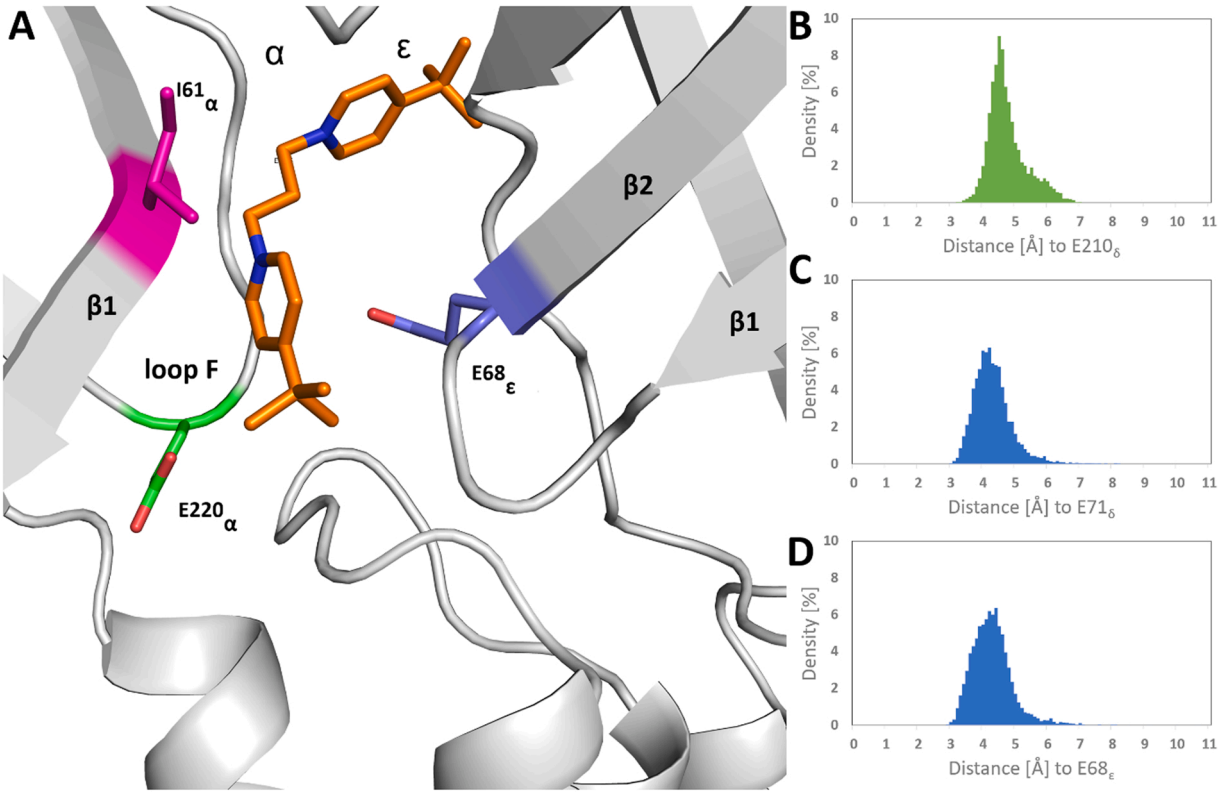


**Fig. 2.** Interactions of MB327 with nAChR in MB327-PAM-1. (A) Proposed binding mode of MB327 in MB327-PAM-1 between the ε- and α-subunits. The color of amino acids $E220_{\alpha}$ and $E68_{\varepsilon}$ relates to the figures in panels B-D. Minimum distance of the nitrogens and carbon atoms located in 4-position of MB327 to the carboxyl oxygens of (B) $E210_{\delta}$ of loop F in the α-δ-subunit (located at the same position as $E220_{\alpha}$, SI Fig. S4 B), (C) $E71_{\delta}$ of the β1-β2-loop in the δ-β-subunit (located at the same position as $E68_{\varepsilon}$, SI Fig. S4 C), and (D) $E68_{\varepsilon}$ of the β1-β2-loop in the α-ε-subunit.

**Table 1**
Sequence similarity of nAChR subunits in various species at specific positions in the MB327-PAM1 binding pockets.[a].

| Human muscle type | | | | α7 | Torpedo marmorata | | | | Rat | | | |
|---|---|---|---|---|---|---|---|---|---|---|---|---|
| α | β | δ | ε | α7 | α | β | δ | γ | α | β | δ | ε |
| *Q* | E | E | E68 | *Q* | *Q* | E | E | E | *Q* | E | E | E |
| E220 | *Q* | E | E | E | E | *Q* | E | E | E | *Q* | E | E |
| I61 | I | I | I | M | I | L | I | I | I | I | I | I |

[a] Amino acids shown in Fig. 2A are represented with green shadings. Amino acids with deviating properties in other subunits are shown in italics.

adjacent subunits through the extracellular β-sheets (Fig. 3B). β-sheets have been demonstrated to be sensitive to changes in structural stability (Whiteley, 2005), and transition pathways along β-sheets have been reported previously (Pfleger et al., 2021, 2017). Especially, the stability of the three β-strands β1, β2, and β6 are affected by MB327 binding. β1 and the β1-β2-loop are both part of MB327-PAM-1. $W78_{\delta}$ in β2 is part of the highly conserved aromatic residues in which nicotine is enveloped according to the cryo-EM structure of the human α3β4-nAChR (PDB ID 6PV7 (Gharpure et al., 2019)). Additionally, via these three β-sheets, MB327 also impacts β7, β9, and β10. The loops of these three β-sheets form the orthosteric binding site. Because MB327 impacts both adjacent subunits, a binding of MB327 to each of the five possible binding pockets likely affects the binding of the orthosteric ligand since each binding site for MB327 features at least one subunit to which the orthosteric ligand binds. This qualitative observation suggests that MB327 addition can modulate cholinergic signals. Hence, we quantified cooperative effects between MB327 and nicotine binding according to Eq. 1 (Pfleger et al., 2021). Our results reveal a positive cooperative effect ($\Delta\Delta G_{CNA,n} = -3.97 \pm 0.71$ kcal mol$^{-1}$), in line with experimental findings that addition of MB327 leads to an enhancement of the cholinergic effect (Niessen et al., 2016). Therefore, binding of MB327 in MB327-PAM-1 is suggested to enhance cholinergic signals by increasing orthosteric ligand affinity.

Notably, a recently published PDB structure of the α7-nAChR (PDB ID 7KOX) shows calcium ions bound in the MB327-PAM-1 pocket (Noviello et al., 2021). Calcium binds in between E44 and E172. E172 is located in loop F, at the same position as $E220_{\alpha}$ (SI Fig. S11). A high concentration of calcium ions increases the cholinergic response in α7-nAChR, and our previous results suggest that the presence of divalent cations enhances the affinity of agonists in Torpedo nAChRs (Niessen et al., 2013; Galzi et al., 1996). Hence, we probed the effect of calcium binding in MB327-PAM-1 on the structural stability of the orthosteric site with CNA. To mimic the presence of the calcium ion which bridges two glutamates, we placed a constraint between the two carboxyl groups of E44 and E172. Similar to MB327, calcium leads to allosteric effects on the orthosteric binding site transmitted via the extracellular β-strands (SI Fig. S12). These findings strengthen the suggestion that positive allosteric modulation of the orthosteric ligand binding can originate

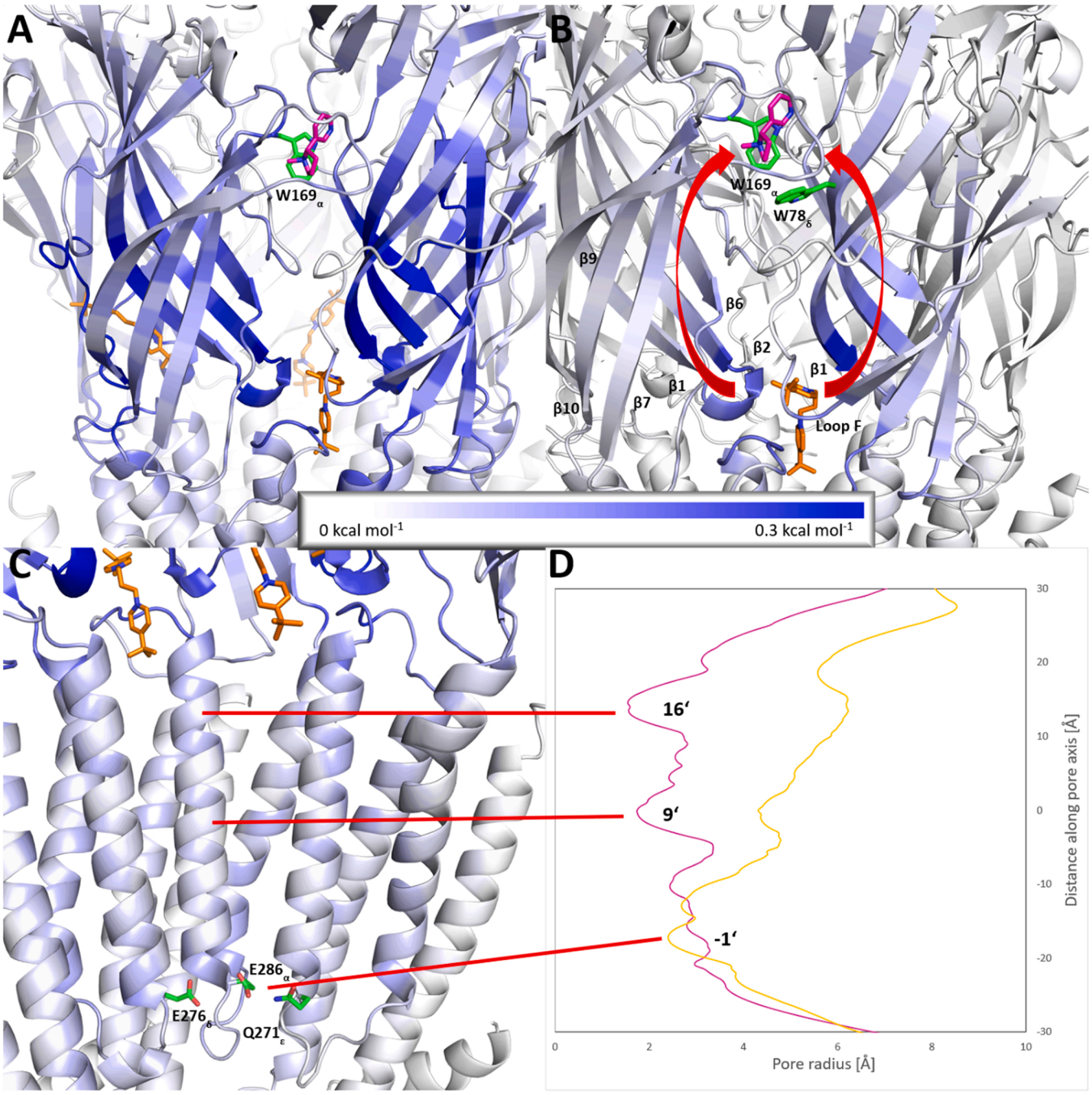


**Fig. 3.** Allosteric effect of MB327 (orange) on nAChR. Effect on the extracellular domain of (A) the three stable MB327 molecules and (B) MB327 located between the alpha- and ε-subunit. The receptor is colored according to the stabilizing impact of MB327 on the respective amino acid (bluish colors); darker colors indicate a higher impact. The pathway of the allosteric stabilization of the orthosteric binding pocket is indicated by red arrows. Nicotine (purple) is shown in the orthosteric binding pocket. $W169_{\alpha}$ and $W78_{\delta}$ are shown in green. (C) Allosteric effects of MB327 on the transmembrane domain of the human muscle type nAChR. For claritiy, only three subunits are shown. Amino acids at position − 1' are shown in green. (D) Pore radii of the desensitized (yellow) and inactive (purple) nAChR. The desensitization gate at position − 1′ and the inactive gates at positions 9′ and 16′ are projected on the structure by red bars. The distance along the pore axis has been set to 0 Å at position 9′.

from binding to MB327-PAM-1.

MB327 binding to MB327-PAM-1 also modulates the structural stability of the transmembrane region, including the amino acids at position − 1′ in helices 2 (Fig. 3C, D). X-ray and cryo-EM structures of nAChRs reveal that this position acts as a desensitization gate (Morales-Perez et al., 2016; Gharpure et al., 2019; Walsh et al., 2018; Noviello et al., 2021). The effects on the position − 1′ ($\Delta G_{E286\alpha,CNA} = 0.075 \pm 0.005$ kcal mol$^{-1}$, $\Delta G_{E276\delta,CNA} = 0.076 \pm 0.004$ kcal mol$^{-1}$, $\Delta G_{Q271\varepsilon,CNA} = 0.041 \pm 0.003$ kcal mol$^{-1}$) are significant. The effect on $W169_{\alpha}$, located at a central position in the orthosteric binding pocket, is even larger ($\Delta G_{W169\alpha,CNA} = 0.224 \pm 0.017$ kcal mol$^{-1}$), which may be due to helices being more stable, and, hence, less receptive to stability changes, in general (Whiteley, 2005). Furthermore, we used the rigidity index to compute $\Delta G_{CNA}$; this index was described to show minor effects on helices (Pfleger et al., 2013b). Overall, the impact on the N-terminal region of helices 2 suggests a mechanism for how MB327 binding reestablishes the muscle function after desensitization, a second effect exerted by MB327 on nAChR (Seeger et al., 2012).

### 3.4. MB327 shows affinity to the orthosteric binding site

Previous results indicate that related bispyridinium compounds transmit their inhibitory effect on nAChR via the orthosteric binding site (Epstein et al., 2021). An inhibitory effect of MB327 has been reported at concentrations above 70 μM (Scheffel et al., 2018). To further investigate a possible binding of MB327 to the orthosteric binding site, we performed ten additional replicas of 900 ns long unbiased free ligand diffusion MD simulations with one MB327 molecule (0.57 mM) placed at a random position within the simulation box around the human muscle-type nAChR. The inhibitory effect of bispyridinium compounds was described to occur via the orthosteric binding site between the α- and ε-subunits (Epstein et al., 2021). Thus, in order to observe a potential binding to this binding site, the orthosteric ligand nicotine was only placed in the orthosteric binding site between the α- and δ-subunits. In three out of ten replicas, MB327 entered the orthosteric binding pocket. In two replicas, MB327 stayed within the binding pocket until the end of the simulation (after its entrance at 54 and 760 ns). In both replicas, MB327 can interact with $Y131_{\varepsilon}$ after binding (Fig. 4A, B), which is important for the stabilization of bispyridinium compounds (Epstein et al., 2021). In the third replica, MB327 bound to the binding pocket after 211 ns and left it after additional 130 ns. However, in this replica, MB327 showed a slightly different binding mode not interacting with $Y131_{\varepsilon}$ (SI Fig. S13).

We also analyzed the electrostatics surrounding the orthosteric binding pocket by solving the linear Poisson-Boltzmann equation for the human muscle-type nAChR. Since the minimum distance of $W169_{\alpha}$, a central amino acid in the orthosteric binding site, to the membrane is 27 Å, the membrane was neglected in calculating the electrostatic properties around the orthosteric binding site. A strong electric field

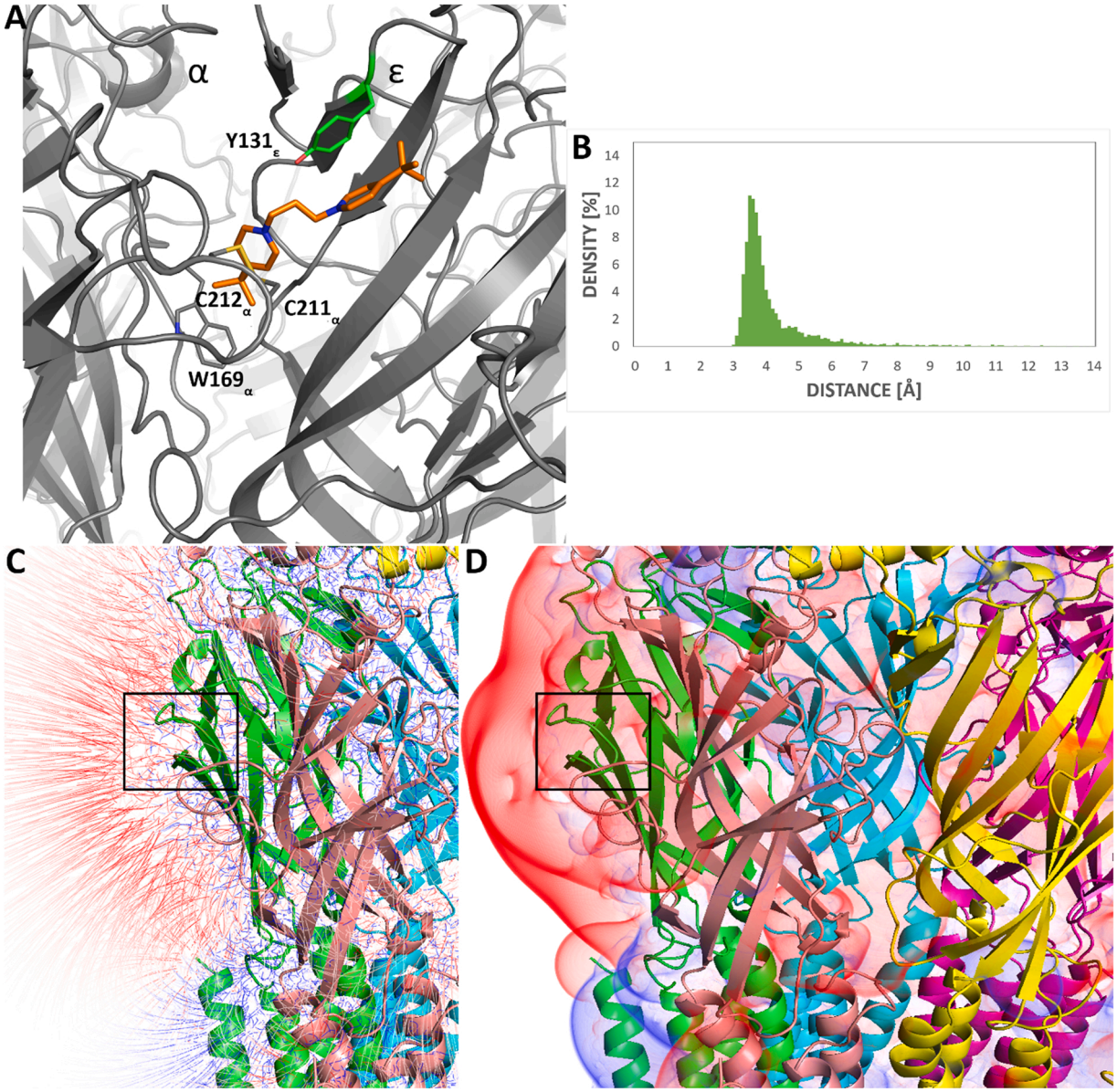


**Fig. 4.** Affinity of MB327 to the orthosteric binding site of nAChR. (A) Representative structure of MB327 (orange) bound to the orthosteric binding pocket and its adjacent region in between the α- and ε-subunit where no nicotine molecule was present during free ligand diffusion MD simulations. (B) Minimum distance of the heavy atoms of the aromatic ring of $Y131_{\varepsilon}$ as shown in (A) to the heavy atoms of the aromatic systems of MB327 while MB327 is bound. Electrostatics surrounding the orthosteric binding pocket between the α- (green) and ε- (salmon) subunits shown as (C) electric flux lines and (D) isocontour surfaces of the electrostatic potential. The location of the orthosteric binding pocket is marked with a black box. Notably, a strong electric field (red field lines) attractive to positively charged compounds such as MB327 surrounds the pocket entrance and leads towards the orthosteric binding pocket of the human nAChR.

attractive to positively charged compounds such as MB327 surrounds the pocket entrance and leads towards the orthosteric binding pocket. This may explain why bispyridinium compounds get dragged into this binding pocket (Fig. 4C,D).

### 3.5. Identification of MB327-PAM-1 allows rational design of more potent analogs

We used the knowledge gained from the binding mode of MB327 in MB327-PAM-1 to predict structural modifications of the ligand that should lead to more potent resensitizers. The *tert*-butyl group of MB327 facing toward the transmembrane domain is located in a polar part of the binding site (Fig. 5A). Thus, substituting the apolar with a polar substituent should increase the binding affinity (Fig. 5B). We, therefore, docked PTM0062 and PTM0063, which carry amino and methylamino groups, (Fig. 5C) in the binding site of all subunits. Both ligands were ranked better than MB327 in all but one subunit, respectively (Fig. 5B, SI Table S5). PTM0062 (**3a**) and PTM0063 (**3b**) were synthesized according to Rappenglück et al. by reacting **1** (Rappenglück, 2018) with pyridin-4-amine (**2a**) and *N*-methylpyridin-4-amine (**2b**), respectively, in acetonitrile under stirring and microwave irradiation for 1 h at 90 °C (Scheme 1) (Rappenglück, 2018). The bispyridinium salts were obtained

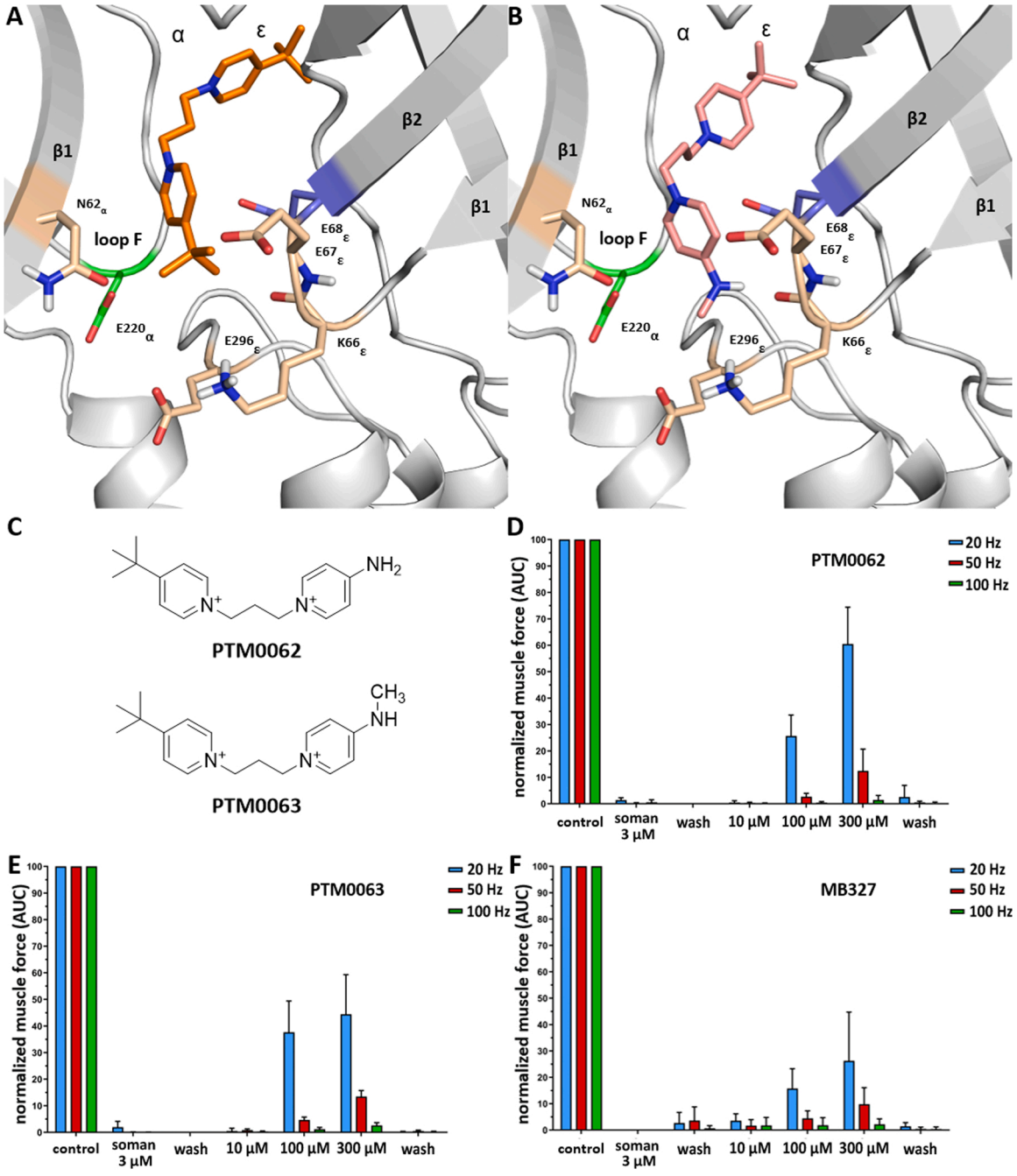


**Fig. 5.** Structure-based ligand design leads to novel compounds with increased resensitizing effects on nAChR. (A) Binding mode of MB327 in between the α- and ε-subunit. The *tert*-butyl substituent facing towards the transmembrane region is located in a polar part of the binding site. (B) Proposed binding mode of PTM0063. Polar substituents can enhance the interactions with the receptor. (C) Structure of the two newly identified positive allosteric modulators PTM0062 and PTM0063. Restoration of the muscle force of soman-poisoned muscles after treatment with (D) PTM0062, (E) PTM0063, and (F) MB327. The error bars indicate the standard deviation.

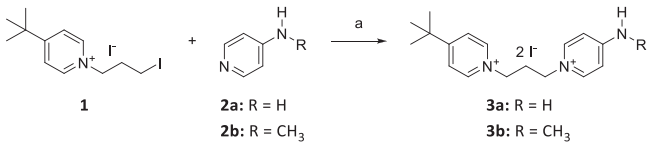


**Scheme 1.** Synthesis of PTM0062 (**3a**) and PTM0063 (**3b**): (a) **2a** (1.1 equiv.) or **2b** (1.05 equiv.), $CH_3CN$, microwave: 150 W, 90 °C, 1 h; **3a**: 82 %; **3b**: 78 %.

in good yields (3a: 82 %; 3b: 78 %) and high purities (> 99 %) by recrystallization of the residues resulting after the removal of the reaction solvent (Scheme 1). The compounds were subsequently evaluated in the rat diaphragm myography assay. PTM0062 (25.68 % ± 7.91 % (mean ± standard deviation) at 100 μM, 60.46 % ± 13.94 % at 300 μM) and PTM0063 (37.65 % ± 11.73 % at 100 μM, 44.43 % ± 14.88 % at 300 μM) both show increased resensitizing effects on muscles after OPC poisoning at a stimulation frequency of 20 Hz compared to MB327 (17.77% ± 7.5 % at 100 μM, 26.29 % ± 18.43 % at 300 μM) (Fig. 5D-F).

## 4. Discussion

We have identified a new potential binding site of MB327 in nAChR, MB327-PAM-1, using blind docking, MD simulations, and rigidity analyses. Previously, two allosteric and one orthosteric binding pocket were proposed for bispyridinium compounds using *in silico* methods (Wein et al., 2018; Epstein et al., 2021). MB327-PAM-1 is different from these three binding sites. Wein et al. suggested that MB327 might bind in between two adjacent subunits in the extracellular domain (MB327–1) or at the transition from the extracellular to the transmembrane domain (MB327–2) (Wein et al., 2018). In our blind dockings, we could also see a binding in the pocket MB327–1 but with worse docking scores compared to our newly identified binding pocket (SI Table S1). In the screening conducted to identify MB327–2, the structure of the *Torpedo marmorata* nAChR (PDB ID 2BG9 (Unwin, 2005)) was used (Wein et al., 2018). However, recently published structures and disulfide trapping experiments revealed that due to the structure's low resolution, the amino acids in the transmembrane domain were wrongly fitted, resulting in an amino acid shift (SI Fig. S14, SI Table S6) (Mnatsakanyan and Jansen, 2013; Morales-Perez et al., 2016). Without this shift, there is no MB327–2 pocket in nAChR (Wein et al., 2018).

During the MD simulations, MB327 is mainly stabilized via electrostatic interactions with glutamates located in the β1-β2 loop and loop F ($E220_{\alpha}$ and $E68_{\varepsilon}$ in Fig. 2A). These two amino acids are highly conserved among different subunits of the nAChR and different species. This corresponds to MB327 showing functional recovery of different types of nAChRs after overstimulation with agonists (Seeger et al., 2012; Niessen et al., 2016). Our newly identified binding pocket also occupies a region in which structural changes during desensitization occur (SI Fig. S15), which suggests that this binding site can be involved in allosteric modulation. Furthermore, CNA calculations show that MB327 might impact both the orthosteric binding site and the transmembrane domain after binding to MB327-PAM-1.

Several published structures of nAChRs and related Cys-loop receptors include allosteric modulators (Zhao et al., 2021; Noviello et al., 2021; Masiulis et al., 2019; Kim et al., 2020; Delbart et al., 2018; Spurny et al., 2013, 2015). A recent structure revealed that the binding site of a calcium ion overlaps with MB327-PAM-1 (Noviello et al., 2021). Calcium can act as a positive allosteric modulator of the α7-nAChR (Galzi et al., 1996). Additionally, mutating E172 of loop F to lysine in the α7-nAChR, which is located at the same position as $E220_{\alpha}$, leads to a loss of sensitivity to the orthosteric ligand acetylcholine (Zhang et al., 2015). A mutation of this amino acid in the α7-nAChR to glutamine also abolishes the enhancement of the physiological response to acetylcholine mediated through calcium ions (Galzi et al., 1996). These data underline the potential importance of this binding pocket in allosteric modulation. Mimicking the calcium ion in this binding pocket by including its interactions into the constraint network representation results in similar effects on the receptor as MB327 as shown with CNA computations. Notably, the calcium ion also exerts a similar effect on the transmembrane region, indicating that calcium might have a resensitizing effect on nAChR, too (SI Fig. S12).

Notably, the binding site of PNU-120596 has been revealed in an electron microscopy structure (PDB-ID: 7EKT (Zhao et al., 2021)) recently. This binding site overlaps with the newly identified allosteric binding site of diazepam in the $GABA_A$ receptor (PDB-IDs: 6X3X (Kim et al., 2020), 6HUP (Masiulis et al., 2019)). Because PNU-120596 also acts as a positive allosteric modulator (Hurst et al., 2005), we investigated whether MB327 may bind to this binding site. However, in the published PDB structure, no negatively charged amino acids are located within 5 Å of PNU-120596, which would lead to an insufficient stabilization of the double positively charged compound MB327 (SI Fig. S16A). Furthermore, PNU-120596 is a selective α7 modulator (Hurst et al., 2005). A reason for that may be that A298 is mutated to sterically larger amino acids in different subtypes of the receptor, which leads to a clash with PNU-120596. Thus, the binding site is critically smaller in other subtypes, including the human muscle-type nAChR (Fig. S16B). However, MB327 is known to bind to several subtypes of nAChR, including the muscle-type nAChR (Turner et al., 2011; Seeger et al., 2012; Niessen et al., 2016; Scheffel et al., 2018; Sichler et al., 2018). Therefore, binding of MB327 to the binding site of PNU-120596 is highly unlikely.

Furthermore, the multitude of binding sites and possible interactions within one binding site in the human muscle-type nAChR could lead to MB327 binding at lower concentrations to MB327-PAM-1 than to the orthosteric binding site. The binding of MB327 to the orthosteric binding pocket results in a binding pose where MB327 protrudes in part out of the pocket, but it completely fits into MB327-PAM-1. After poisoning with OPCs resulting in elevated levels of acetylcholine, MB327 would additionally need to displace acetylcholine in the orthosteric binding pocket because the binding pose of MB327 in the orthosteric pocket overlaps with the binding pose of the orthosteric ligand. Thus, binding to the orthosteric site would be expected at higher concentrations, where it can lead to an inhibitory effect. This inhibitory effect was shown by us in that an increase of MB327 concentration leads to a decrease of muscle force restoration after soman poisoning (Niessen et al., 2018). Furthermore, recent mutational studies showed that related bispyridinium compounds transfer their inhibitory effect via binding to the orthosteric pocket (Epstein et al., 2021).

Epstein et al. proposed that the therapeutic effect of bispyridinium compounds could be conducted via binding to the orthosteric binding site and its adjacent region (Epstein et al., 2021). We also see an affinity of MB327 to this binding site in our free ligand diffusion MD simulations. Epstein et al. performed docking experiments considering the orthosteric binding pocket and did not investigate binding to allosteric binding pockets. However, previous experimental results indicate that the bispyridinium compounds probably act as allosteric modulators of nAChR and, additionally, improvement of neuromuscular function is not correlated to their affinity to the orthosteric binding site (Niessen et al., 2016, 2018, 2011). Thus, although an inhibitory effect, detrimental to the therapeutic treatment, of the bispyridinium compounds might be conducted through binding to the orthosteric binding site at higher concentrations (Epstein et al., 2021; Niessen et al., 2018), our results suggest that for the allosteric modulation, relevant for treatment, MB327 binds to the newly identified binding pocket. This concentration-dependent binding to the allosteric and orthosteric binding site can also explain the therapeutic effect seen at lower concentrations of MB327 and the inhibition of the nAChR and loss of therapeutic effect at higher concentrations (Niessen et al., 2018). Thus, our results suggest that new drugs should show a high affinity to the newly identified binding pocket while showing a low affinity to the orthosteric binding site.

The knowledge of the binding mode is most important to predict

structure-based ligand modifications resulting in more potent resensitzers. Following this strategy, we predicted and validated PTM0062 and PTM0063, which are about two-fold more potent resensitizers than MB327. These findings further support that MB327 binds to MB327-PAM-1. Another way to enhance the affinity to the newly identified binding site might be to add chemical moieties that can form interactions via hydrogen bonds or salt bridges to the two glutamates $E220_{\alpha}$ and E68ε, while maintaining the apolar part of the compounds.

Taken together, our newly identified binding pocket can explain the allosteric effect mediated by MB327 and, together with a binding to the orthosteric site, the concentration dependence of the observed therapeutic effect.

## Declaration of Competing Interest

The authors declare that they have no known competing financial interests or personal relationships that could have appeared to influence the work reported in this paper.

## Data availability

Data will be made available on request.

## Acknowledgments

This work was supported by the German Ministry of Defense (E/U2AD/KA019/IF558). We are grateful for computational support and infrastructure provided by the "Zentrum für Informations- und Medientechnologie" (ZIM) at the Heinrich Heine University Düsseldorf and the computing time provided by the John von Neumann Institute for Computing (NIC) to HG on the supercomputer JUWELS at Jülich Supercomputing Center (JSC) (user IDs: HKF7, VSK33, nAChR). HG is grateful to OpenEye Scientific Software for granting a Free Public Domain Research License.

## Appendix A. Supporting information

Supplementary data associated with this article can be found in the online version at doi:10.1016/j.toxlet.2022.11.018.

## References

Altschul, S.F., et al., 1990. Basic local alignment search tool. J. Mol. Biol. 215 (3), 403–410.
Bayly, C.I., et al., 1993. A well-behaved electrostatic potential based method using charge restraints for deriving atomic charges: the RESP model. J. Phys. Chem. 97 (40), 10269–10280.
Case, D.A., et al., 2005. The Amber biomolecular simulation programs. J. Comput. Chem. 26 (16), 1668–1688.
Celie, P.H., et al., 2004. Nicotine and carbamylcholine binding to nicotinic acetylcholine receptors as studied in AChBP crystal structures. Neuron 41 (6), 907–914.
Cushman, M., et al., 2014. Absolute quantitative (1)h NMR spectroscopy for compound purity determination. J. Med Chem. 57 (22), 9219.
Darden, T., York, D., Pedersen, L., 1993. Particle mesh Ewald: an N·log(N) method for Ewald sums in large systems. J. Chem. Phys. 98 (12), 10089–10092.
OpenEye Scientific Software, I., *SZYBKI*. OpenEye Scientific Software: Santa Fe, NM.
Delbart, F., et al., 2018. An allosteric binding site of the alpha7 nicotinic acetylcholine receptor revealed in a humanized acetylcholine-binding protein. J. Biol. Chem. 293 (7), 2534–2545.
Dittrich, J., et al., 2019. Converging a knowledge-based scoring function: drugscore (2018). J. Chem. Inf. Model. 59 (1), 509–521.
Epstein, M., et al., 2021. Molecular determinants of binding of non-oxime bispyridinium nerve agent antidote compounds to the adult muscle nAChR. Toxicol. Lett. 340, 114–122.
M.J. Frisch, G.W.T, H.B. Schlegel, G.E. Scuseria, et al., Gaussian16. 2016, Gaussian Inc.: Wallingford CT.
Galzi, J.L., et al., 1996. Identification of calcium binding sites that regulate potentiation of a neuronal nicotinic acetylcholine receptor. EMBO J. 15 (21), 5824–5832.
Gharpure, A., et al., 2019. Agonist selectivity and ion permeation in the alpha3beta4 ganglionic nicotinic receptor. Neuron 104 (3), 501–511 e6.
Hibbs, R.E., et al., 2009. Structural determinants for interaction of partial agonists with acetylcholine binding protein and neuronal alpha7 nicotinic acetylcholine receptor. EMBO J. 28 (19), 3040–3051.
Holmstedt, B., 1959. Pharmacology of organophosphorus cholinesterase inhibitors. Pharm. Rev. 11, 567–688.
Hopkins, C.W., et al., 2015. Long-time-step molecular dynamics through hydrogen mass repartitioning. J. Chem. Theory Comput. 11 (4), 1864–1874.
Hurst, R.S., et al., 2005. A novel positive allosteric modulator of the alpha7 neuronal nicotinic acetylcholine receptor: in vitro and in vivo characterization. J. Neurosci. 25 (17), 4396–4405.
Izadi, S., Anandakrishnan, R., Onufriev, A.V., 2014. Building water models: a different approach. J. Phys. Chem. Lett. 5 (21), 3863–3871.
Jurrus, E., et al., 2018. Improvements to the APBS biomolecular solvation software suite. Protein Sci. 27 (1), 112–128.
Kim, J.J., et al., 2020. Shared structural mechanisms of general anaesthetics and benzodiazepines. Nature 585 (7824), 303–308.
Lomize, M.A., et al., 2012. OPM database and PPM web server: resources for positioning of proteins in membranes. Nucleic Acids Res. 40 (Database issue), D370–D376.
Masiulis, S., et al., 2019. GABAA receptor signalling mechanisms revealed by structural pharmacology. Nature 565 (7740), 454–459.
Miller 3rd, B.R., et al., 2012. MMPBSA.py: an efficient program for end-state free energy calculations. J. Chem. Theory Comput. 8 (9), 3314–3321.
Mnatsakanyan, N., Jansen, M., 2013. Experimental determination of the vertical alignment between the second and third transmembrane segments of muscle nicotinic acetylcholine receptors. J. Neurochem. 125 (6), 843–854.
Morales-Perez, C.L., Noviello, C.M., Hibbs, R.E., 2016. X-ray structure of the human alpha4beta2 nicotinic receptor. Nature 538 (7625), 411–415.
Morris, G.M., et al., 1998. Automated docking using a Lamarckian genetic algorithm and an empirical binding free energy function. J. Comput. Chem. 19 (14), 1639–1662.
Mukherjee, S., et al., 2020. Synthetic antibodies against BRIL as universal fiducial marks for single-particle cryoEM structure determination of membrane proteins. Nat. Commun. 11 (1), 1598.
Mulnaes, D., Gohlke, H., 2018. TopScore: using deep neural networks and large diverse data sets for accurate protein model quality assessment. J. Chem. Theory Comput. 14 (11), 6117–6126.
Niessen, K.V., et al., 2011. Interaction of bispyridinium compounds with the orthosteric binding site of human alpha7 and Torpedo californica nicotinic acetylcholine receptors (nAChRs). Toxicol. Lett. 206 (1), 100–104.
Niessen, K.V., et al., 2013. Affinities of bispyridinium non-oxime compounds to [(3)H] epibatidine binding sites of Torpedo californica nicotinic acetylcholine receptors depend on linker length. Chem. Biol. Interfaces 206 (3), 545–554.
Niessen, K.V., et al., 2016. Functional analysis of Torpedo californica nicotinic acetylcholine receptors in multiple activation states by SSM-based electrophysiology. Toxicol. Lett. 247, 1–10.
Niessen, K.V., et al., 2018. In vitro pharmacological characterization of the bispyridinium non-oxime compound MB327 and its 2- and 3-regioisomers. Toxicol. Lett. 293, 190–197.
Noviello, C.M., et al., 2021. Structure and gating mechanism of the alpha7 nicotinic acetylcholine receptor. Cell 184 (8), 2121–2134 e13.
OpenEye Scientific Software, I., OEDOCKING. 2020. Santa Fe, NM.
OpenEye Scientific Software, I., OMEGA. 2020. Santa Fe, NM.
Olsson, M.H., et al., 2011. PROPKA3: consistent treatment of internal and surface residues in empirical pKa predictions. J. Chem. Theory Comput. 7 (2), 525–537.
Onufriev, A., Bashford, D., Case, D.A., 2004. Exploring protein native states and large-scale conformational changes with a modified generalized born model. Proteins 55 (2), 383–394.
Pauli, G.F., et al., 2014. Importance of purity evaluation and the potential of quantitative (1)H NMR as a purity assay. J. Med. Chem. 57 (22), 9220–9231.
Pavelka, A., et al., 2016. CAVER: algorithms for analyzing dynamics of tunnels in macromolecules. IEEE/ACM Trans. Comput. Biol. Bioinform. 13 (3), 505–517.
Pei, J., Kim, B.H., Grishin, N.V., 2008. PROMALS3D: a tool for multiple protein sequence and structure alignments. Nucleic Acids Res. 36 (7), 2295–2300.
Pettersen, E.F., et al., 2004. UCSF Chimera – a visualization system for exploratory research and analysis. J. Comput. Chem. 25 (13), 1605–1612.
Pfleger, C., et al., 2013a. Constraint network analysis (CNA): a python software package for efficiently linking biomacromolecular structure, flexibility, (thermo-)stability, and function. J. Chem. Inf. Model. 53 (4), 1007–1015.
Pfleger, C., et al., 2013b. Global and local indices for characterizing biomolecular flexibility and rigidity. J. Comput. Chem. 34 (3), 220–233.
Pfleger, C., et al., 2017. Ensemble- and rigidity theory-based perturbation approach to analyze dynamic allostery. J. Chem. Theory Comput. 13 (12), 6343–6357.
Pfleger, C., et al., 2021. Allosteric signaling in C-linker and cyclic nucleotide-binding domain of HCN2 channels. Biophys. J. 120 (5), 950–963.
Rahman, M.M., et al., 2020. Structure of the native muscle-type nicotinic receptor and inhibition by snake venom toxins. Neuron 106 (6), 952–962 e5.
Rappenglück, S., et al., 2018. Synthesis of a series of non-symmetric bispyridinium and related compounds and their affinity characterization at the nicotinic acetylcholine receptor. ChemMedChem 13 (24), 2653–2663.
Roe, D.R., Cheatham 3rd, T.E., 2013. PTRAJ and CPPTRAJ: software for processing and analysis of molecular dynamics trajectory data. J. Chem. Theory Comput. 9 (7), 3084–3095.
Ryckaert, J.-P., Ciccotti, G., Berendsen, H.J.C., 1977. Numerical integration of the cartesian equations of motion of a system with constraints: molecular dynamics of n-alkanes. J. Comput. Phys. 23 (3), 327–341.
Scheffel, C., et al., 2018. Electrophysiological investigation of the effect of structurally different bispyridinium non-oxime compounds on human alpha7-nicotinic acetylcholine receptor activity – an in vitro structure-activity analysis. Toxicol. Lett. 293, 157–166.

Schott-Verdugo, S., Gohlke, H., 2019. PACKMOL-Memgen: a simple-to-use, generalized workflow for membrane-protein-lipid-bilayer system building. J. Chem. Inf. Model. 59 (6), 2522–2528.
Schrödinger, L.L.C., The PyMOL Molecular Graphics System, *Version 1.8*., 2015.
Schrödinger, L.L.C., Maestro. 2020.
Seeger, T., et al., 2007. Reevaluation of indirect field stimulation technique to demonstrate oxime effectiveness in OP-poisoning in muscles in vitro. Toxicology 233 (1–3), 209–213.
Seeger, T., et al., 2012. Restoration of soman-blocked neuromuscular transmission in human and rat muscle by the bispyridinium non-oxime MB327 in vitro. Toxicology 294 (2–3), 80–84.
Shen, M.Y., Sali, A., 2006. Statistical potential for assessment and prediction of protein structures. Protein Sci. 15 (11), 2507–2524.
Sheridan, R.D., et al., 2005. Nicotinic antagonists in the treatment of nerve agent intoxication. J. R. Soc. Med. 98 (3), 114–115.
Sichler, S., et al., 2018. Development of MS Binding Assays targeting the binding site of MB327 at the nicotinic acetylcholine receptor. Toxicol. Lett. 293, 172–183.
Sondergaard, C.R., et al., 2011. Improved treatment of ligands and coupling effects in empirical calculation and rationalization of pKa values. J. Chem. Theory Comput. 7 (7), 2284–2295.
Spurny, R., et al., 2013. Multisite binding of a general anesthetic to the prokaryotic pentameric Erwinia chrysanthemi ligand-gated ion channel (ELIC). J. Biol. Chem. 288 (12), 8355–8364.
Spurny, R., et al., 2015. Molecular blueprint of allosteric binding sites in a homologue of the agonist-binding domain of the alpha7 nicotinic acetylcholine receptor. Proc. Natl. Acad. Sci. USA 112 (19), E2543–E2552.
Thiermann, H., Worek, F., Kehe, K., 2013. Limitations and challenges in treatment of acute chemical warfare agent poisoning. Chem. Biol. Interfaces 206 (3), 435–443.
Tian, C., et al., 2020. ff19SB: amino-acid-specific protein backbone parameters trained against quantum mechanics energy surfaces in solution. J. Chem. Theory Comput. 16 (1), 528–552.
Turner, S.R., et al., 2011. Protection against nerve agent poisoning by a noncompetitive nicotinic antagonist. Toxicol. Lett. 206 (1), 105–111.
Twizerimana, A.P., et al., 2020. Cell type-dependent escape of capsid inhibitors by simian immunodeficiency virus SIVcpz. J. Virol. 94 (23).
Unwin, N., 2005. Refined structure of the nicotinic acetylcholine receptor at 4A resolution. J. Mol. Biol. 346 (4), 967–989.
Unwin, N., Fujiyoshi, Y., 2012. Gating movement of acetylcholine receptor caught by plunge-freezing. J. Mol. Biol. 422 (5), 617–634.
Walsh Jr., R.M., et al., 2018. Structural principles of distinct assemblies of the human alpha4beta2 nicotinic receptor. Nature 557 (7704), 261–265.
Webb, B., Sali, A., 2016. Comparative protein structure modeling using MODELLER. Curr. Protoc. Bioinform. 54 (5 6 1-5 6 37).
Wein, T., et al., 2018. Searching for putative binding sites of the bispyridinium compound MB327 in the nicotinic acetylcholine receptor. Toxicol. Lett. 293, 184–189.
Whiteley, W., 2005. Counting out to the flexibility of molecules. Phys. Biol. 2 (4), S116–S126.
Wiener, S.W., Hoffman, R.S., 2004. Nerve agents: a comprehensive review. J. Intensive Care Med. 19 (1), 22–37.
Worek, F., Thiermann, H., Szinicz, L., 2004. Reactivation and aging kinetics of human acetylcholinesterase inhibited by organophosphonylcholines. Arch. Toxicol. 78 (4), 212–217.
Zhang, Q., et al., 2015. Functional impact of 14 single nucleotide polymorphisms causing missense mutations of human alpha7 nicotinic receptor. PLOS One 10 (9), e0137588.
Zhao, Y., et al., 2021. Structural basis of human α7 nicotinic acetylcholine receptor activation. Cell Res. 31 (6), 713–716.